Journal of Nuclear Materials 557 (2021) 153281

Contents lists available at ScienceDirect

Journal of Nuclear Materials

journal homepage: www.elsevier.com/locate/jnucmat

# Emulation of neutron damage with proton irradiation and its effects on microstructure and microchemistry of Zircaloy-4

Peng Wang[a,*], Josh Bowman[b], Mukesh Bachhav[c], Bruce Kammenzind[d], Richard Smith[d], Jesse Carter[d], Arthur Motta[b], Evrard Lacroix[e], Gary Was[a]

[a] Nuclear Engineering and Radiological Sciences, University of Michigan, Ann Arbor, MI 48109, USA
[b] Department of Mechanical and Nuclear Engineering, Pennsylvania State University, University Park, PA 16802, USA
[c] Idaho National Laboratory, Materials and Fuel Complex, Idaho Falls, ID, USA
[d] Naval Nuclear Laboratory, Bettis Laboratory, PO box 79, West Mifflin PA 15122, USA
[e] Framatome Inc., Old Forest Road, Lynchburg, VA 24501, USA

ARTICLE INFO

*Article history:*
Received 5 May 2021
Revised 23 July 2021
Accepted 1 September 2021
Available online 4 September 2021

ABSTRACT

This work assesses the potential of proton irradiation to simulate the neutron damage to the matrix and laves phase $Zr(Fe,Cr)_2$ precipitates in Zircaloy-4. Isothermal proton irradiation has been performed on Zircaloy-4 samples at irradiation temperatures ranging from 250 to 350 °C. Two-step proton irradiation was also performed to enhance the amorphization of and iron loss from the laves phase $Zr(Fe,Cr)_2$ precipitates. The irradiated microstructures, including dislocation loops and rafts near SPPs, were observed in proton irradiated Zircaloy-4, which are consistent with neutron irradiated material at a similar damage level. The amount of irradiation-induced hardening after proton irradiation was similar to post neutron irradiated data. The significant amorphization of the SPPs and concurrent Fe redistribution observed on neutron irradiated materials can be effectively emulated using a two-step proton irradiation on Zircaloy-4. Hence, the neutron irradiation effect on Zircaloy-4 can be mostly captured using the two-step proton irradiation described in this study.



## 1. Introduction

This work is being conducted as a part of the Mechanistic Understanding of Zirconium Corrosion MUZIC-3 Consortium, investigating irradiation-induced corrosion acceleration mechanisms in zirconium base alloys. As discussed in detail in Ref. [1], the long-term post-transition corrosion rates of Zircaloy-4 are significantly accelerated in a PWR radiation environment over that observed with non-irradiated specimens in an autoclave environment. In-reactor post-transition corrosion rate acceleration by as much as 30 to 40 times that of long-term out-of-reactor autoclave rates are observed at irradiation temperatures of ~270 °C to 310 °C. This in-reactor acceleration decreases with increasing irradiation temperature, becoming only a factor of ~3 to 4 times the long-term autoclave corrosion rates at 350 °C [1]. As a result, there is a greater in-reactor corrosion acceleration at low temperatures.

Interestingly, as illustrated in Ref. [1], the PWR radiation environment has little effect on the pre-transition corrosion rates of Zircaloy-4, even after extended times in the environment, over 1200 days at 270 °C, under neutron flux conditions as high as $1 \times 10^{14}$ neutrons/cm$^2$-s (E>1 MeV) and to damage levels as high as 17 dpa. This indicates that displacement interactions of neutron irradiation with the growing pre-transition oxide film itself do not significantly affect the rate-limiting transport processes of oxygen and electrons through this passivating layer, approximately half of which was established in autoclave pre-filming. The relative insensitivity of Zircaloy pretransition corrosion to irradiation in the PWR environment is consistent with the uncertainty in the literature about whether the radiation environment of a PWR caused any acceleration of Zircaloy corrosion [2]. This observation is also consistent with recent short-time *in-situ* proton irradiation corrosion tests, showing no measurable corrosion acceleration of Zircaloy-4 under proton irradiation conditions simulating dpa rates occurring under high-flux neutron-irradiation conditions in a PWR environment, $\sim 1.7 \times 10^{-7}$ dpa/s [3]. It is not surprising that significant enhancement is not instantaneous. It requires some period before fully manifesting itself since such a low damage rate would require significant irradiation time to accumulate enough dose to show a microstructure or microchemistry shift from the non-irradiated materials.

The corrosion data presented in Kammenzind et al. [1] indicate that two factors significantly increase the observed in-reactor cor-

* Corresponding author.

https://doi.org/10.1016/j.jnucmat.2021.153281
0022-3115/

rosion rates of Zircaloy over that observed in an autoclave. One is pre-irradiation of the Zircaloy metal, and the second is applying a thicker post-transition corrosion film before insertion into the in-reactor environment. Indeed, several other factors (as reviewed by Cox [4]) can contribute to the enhanced post-transition corrosion rates observed in-reactor on Zircaloy-4 clad fuel rods. These factors include high hydride concentration at the surface of rods near end-of-life [5–8] and potential concentration of lithium from the bulk water into the corrosion film as a result of boiling within the film [9–11]. While these effects must be accounted for to accurately model the overall corrosion behavior of Zircaloy clad fuel elements, they are not direct effects of the radiation environment but more from heat transfer out of the fuel rods. Such effects can be duplicated in out-of-reactor environments. The hydride and lithium effects mentioned above are absent from the Advanced Test Reactor (ATR) test samples [1], as there is virtually no heat flux emanating from them, and hydrogen contents of the samples are relatively low, even after fluences of greater than $100 \times 10^{24}$ n/m$^2$ in the high flux, 270 °C to 310 °C temperature environments. Thus the large corrosion accelerations observed in Zircaloy-4 in Ref. [1] directly result from the radiation environment.

It is well known that extended neutron irradiation alters the starting non-irradiated microstructure and microchemistry of Zircaloy-4 in several ways. The high-fluence effects of neutron irradiation on the base metal have been demonstrated to affect corrosion rates in post-irradiation autoclave corrosion tests [12,13]. Its impact is accentuated in the in-reactor environment [1], where sustained corrosion acceleration (especially once a post-transition corrosion film with a porous outer oxide layer develops) is much more significant than observed in the post-irradiation autoclave exposures (without the irradiation environment). As demonstrated by Kammenzind et al. [1], the fact that the presence of a fossil oxide film on the surface of previously non-irradiated corroding samples accelerates the in-reactor corrosion of zirconium alloys in its own right, combined with the observation that this acceleration is increased with increasing fluence as second phase particles (SPPs) in the Zircaloy-4 metal are altered by irradiation suggests that *some aspects of the radiation environment are acting synergistically with the corrosion film formed from the irradiation damaged base metal to accelerate corrosion rates further in-reactor.*

The overall goal of this program is to utilize proton irradiation as one tool to separate the effect of irradiation damage to the metal on the accelerated corrosion from the effects of heterogeneous radiolysis within the fossil oxide discussed in Ref. [1,14]. Proton irradiation has been used in the past to study the mechanical response of zirconium alloys in lieu of neutron irradiation due to its quick turnaround time and low activation of the metal [15–18]. More detailed comparisons between ion and neutron irradiation are unfortunately beyond the scope of this article. However, detailed discussions on this topic are available elsewhere [19–21]. Although previous studies have demonstrated its feasibility in inducing loop formation and simulating post-neutron-irradiated mechanical behavior, only a limited number of these studies explored the post-irradiation microstructure and microchemistry of the SPPs or the effect of irradiation conditions on their evolution. A good summary of what has been published can be found in Ref. [22]. However, as summarized above and discussed in Ref. [1], it is the SPP microstructural and microchemical evolution that is hypothesized to be a critical factor in the corrosion performance of Zircaloy-4 in a PWR environment. Hence, this work explores the use of proton irradiation to emulate neutron damage of the microstructural and microchemical evolution of the SPPs and matrix in Zircaloy-4. From the experiments, the best proton irradiation conditions and practices are the two-step irradiation that reproduced the microstructural and microchemical evolutions that represent the neutron irradiation of Zircaloy-4 in a PWR environment.

**Table 1**
Chemical composition of recrystallized Zircaloy-4 (wt.%) used in this study.

| Alloy | Sn | Fe | Cr | O | Si | Al | H |
|---|---|---|---|---|---|---|---|
| Zircaloy-4 | 1.55 | 0.22 | 0.11 | 0.14 | 0.01 | 0.003 | 0.0005 |

## 2. Experimental

### 2.1. Material and sample fabrication

Fully recrystallized Zircaloy-4 in 1 mm sheet stock was used in this study. The alloy composition of the supplied material is listed in Table 1. The material was processed for corrosion resistance in a PWR environment. All final processing steps for the sheet material were performed in the single alpha-phase field. The final plate received a recrystallization anneal in the high alpha-phase field following rolling. The final annealing parameter "*A*" was approximately $1 \times 10^{-16}$ [23], where *A* is defined as

$$A = \sum t_i \exp\left(-40,000/T_i\right) \quad (1)$$

where $t_i$ is the time of annealing step $i$ in hours, and $T_i$ is the temperature of annealing step $i$ in Kelvin. This processing produced second phase precipitates with a mean size on the order of 0.24 µm. The final material has equiaxed grains with a mean grain size of about 15 µm. The material was specially prepared, and the grain size has been verified. The final texture represents alpha-phase rolled and annealed plate product with the majority of the basal poles perpendicular to the plate surface, split up to 30° in the transverse direction. This material received the same processing and has the same starting microstructure as the specimens discussed in Refs. [1] and [24]. The starting microstructure and composition of the SPPs are more fully described in Ref. [25].

Matchstick-size bars of geometry $2 \times 20 \times 1$ mm were produced out of the sheet stock using electric discharge machining (EDM). The as-cut surfaces after EDM were removed by mechanical grinding using silicon carbide sandpaper, and the surfaces subject to irradiation are further polished to a mirror finish using colloidal silica.

### 2.2. Proton irradiation experiment

The Zircaloy-4 samples were proton irradiated at the Michigan Ion Beam Laboratory using a 3 MV Pelletron accelerator. A 2 MeV proton beam was delivered to the sample surface at a current density of 41 µA/cm$^2$ ($2.6 \times 10^{14}$ protons/cm$^2$-s). Multiple irradiations were carried out at various temperatures to study the effects of irradiation temperature on alloy microstructure evolution. SRIM was employed to simulate displacement damage events in the target material using 2 MeV protons as projectiles. The Quick Kinchin-Pease mode was applied in this study, as Stoller et al. [26] recommended, with a displacement energy of 40 eV for Zr, Fe, and Cr. The proton irradiation dose (dpa) level was calculated at a depth of 3-5 µm below the irradiated surface. At this penetration depth, a proton fluence of $7.8 \times 10^{19}$ protons/cm$^2$ would impart about 5 dpa of damage to the sample at a damage rate of $\sim 1.62 \times 10^{-5}$ dpa/s, which is about two orders of magnitude greater than peak damage rates experienced as a result of neutron irradiation in a PWR environment. The calculated proton damage profile and proton distribution profile are illustrated in Fig. 1.

Several proton irradiations were conducted in this study; five isothermal irradiations (250 °C, 280 °C, 310 °C, 330 °C, and 350 °C) and two-step irradiation that involves the first half being carried

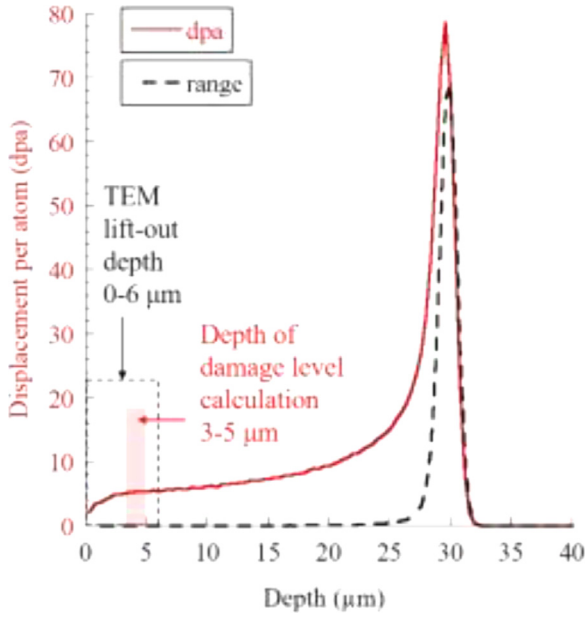


**Fig. 1.** SRIM simulated proton range probability and damage profile for 2 MeV protons in Zr. This calculation was done using the Quick Kinchin-Pease option of SRIM 2008 [27], with the displacement energy of 40 eV, and assigning a proton fluence of $7.8 \times 10^{19}$ protons/cm$^2$. The dashed box indicates the depth of where the lift-out sample was taken, and the red shaded area represents the depth where the sample damage level was determined (For interpretation of the references to color in this figure legend, the reader is referred to the web version of this article.).

out at low temperature (-10 °C) and the second half being performed at high temperature (350 °C). For each isothermal irradiation temperature, six individual bars were irradiated through the multi-step irradiations to produce a set of samples with three different doses (0.5. 1.6 and 5 dpa). As illustrated in Fig. 2, Zone 1 (highlighted in red) was irradiated to 3.4 dpa in Step 1, with an irradiation area of 6 × 6 mm; followed by opening the left beamline slit up by 6 mm (6 × 12 mm irradiating area), allowing an additional 1.1 dpa to be accumulated in Zones 1 and 2 in Step 2; finished by opening the right slit to the full width (6 × 18 mm), and allowing an additional 0.5 dpa to be accumulated on all three zones. Each irradiation zone consists of two bar samples, bounded by two dummy bars (dark grey) on either side. J-type thermocouples (TC) were attached to the dummy bars to calibrate a 2-D FLIR® Thermal Imaging System that monitored the temperature at multiple locations for each irradiation throughout the experiment to generate a temperature histogram. Temperature control was maintained using an electric cartridge heater and pressurized air cooling of the back of the irradiation stage and yielded an average $2\sigma$ variation of <3 °C. Heat conduction between the stage and the samples was through a layer of molten indium. The vacuum chamber pressure of each irradiation was maintained below $10^{-7}$ torr ($< 1.3 \times 10^{-5}$ Pa).

Two bar samples were irradiated in the two-step irradiations. The -10 °C (2.5 dpa) irradiation was conducted using a dedicated liquid nitrogen cooled irradiation stage. The sample was mounted on a copper block via a layer of indium as the heat conductor. The copper block was thermally insulated and only connected to a liquid-nitrogen-cooled copper rod. The initial temperature of the sample without a proton beam was recorded to be as low as -163 °C. With the proton beam on the sample, the surface temperature rose to -10 °C. Upon completing the low-temperature irradiation part, the irradiated samples were subjected to a high temperature 350 °C (additional 2.5 dpa) irradiation to promote Fe redistribution and dislocation loop formation.

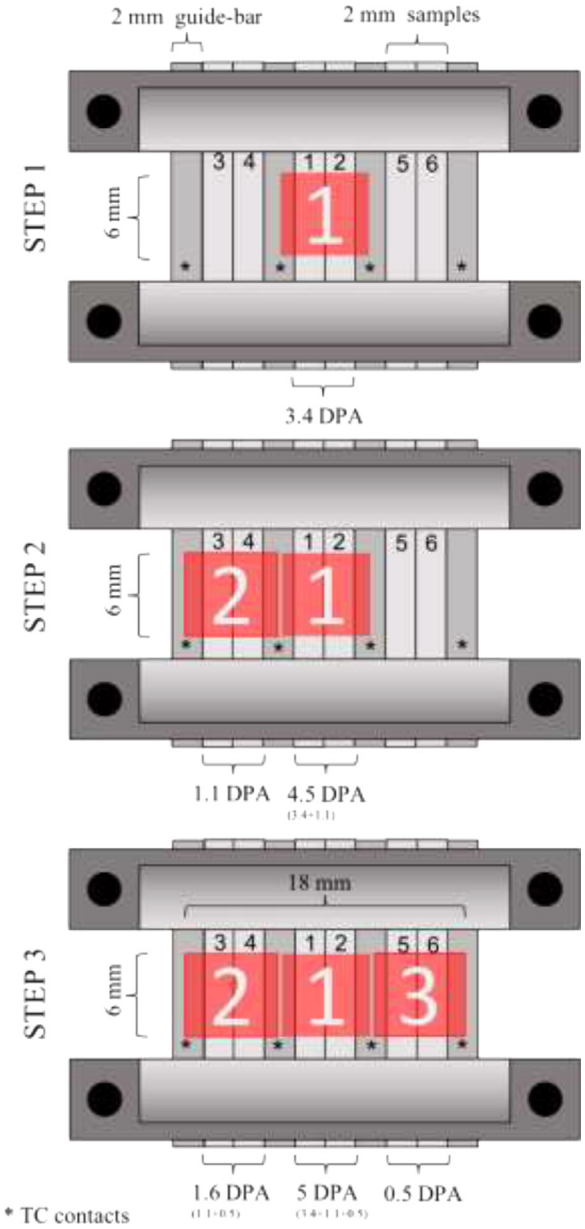


**Fig. 2.** Schematic of sample arrangement and irradiation steps to achieve different dose levels in different egions (For interpretation of the references to color in this figure, the reader is referred to the web version of this article.).

### 2.3. TEM sample preparation

Transmission electron microscopy (TEM) lamellae were prepared in an FEI Helios Nanolab 650 focused ion beam (FIB) system at the Michigan Center for Materials Characterization (MC$^2$) at the University of Michigan. The depth at which the dose level was determined in Section 2.2 was intentionally chosen when considering the future characterization of the irradiated microstructure, as typical FIB lift-out samples are 10–15 μm in width and 5, 6 μm in height. The lift-out taken at 3–5 μm below the surface would be appropriate to represent the damage level determined by the SRIM calculation. For example, the depth range of 3–5 $\mu$m below the surface on a typical lift-out from a 5 dpa sample would represent a microstructure of a sample that received 5 dpa of displacement damage. Lift-out procedures applied in this work consist of two steps. First, a lamella was rough cut and lifted out onto a copper grid. Second, a liquid nitrogen cooled cryo-stage was utilized while

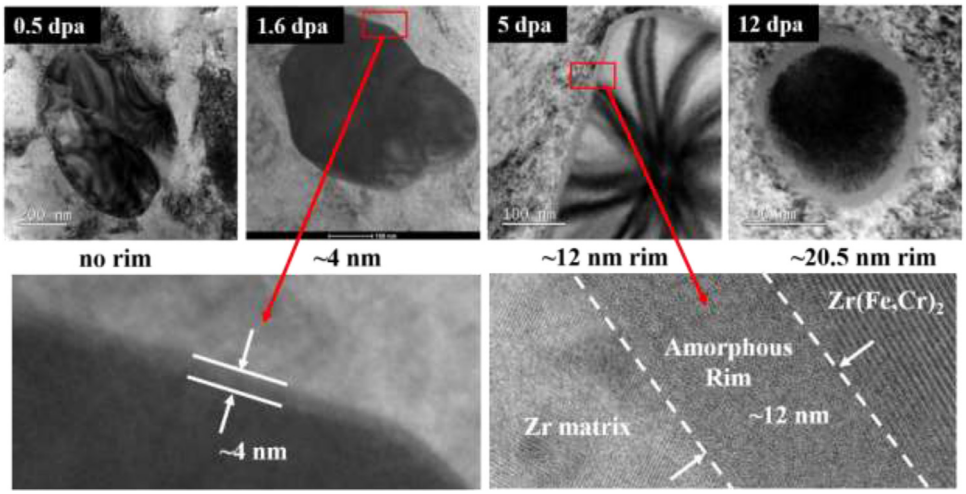


**Fig. 3.** TEM bright-field images of amorphized rim evolution of SPPs as a function of damage level, SPPs in the depth of 3–5 μm below the irradiated surface were examined on the 280 °C proton irradiated samples (0.5, 1.6, and 5 dpa), whereas the 12 dpa SPP was examined in a lift-out that was taken at a depth of 20–25 μm below the irradiated surface on the 5 dpa specimen, near the peak damage region illustrated in Fig. 1.

carrying out the thinning process at -150 °C. The cryogenic temperature stage acts as a cold finger to reduce the hydrogen partial pressure near the sample surface and significantly reduce the kinetics for hydrogen adsorption, absorption, and diffusion. The cryogenic thinning procedure ensures that the TEM lamellae are free of artifact $\delta$ hydride precipitation [28]. The final thinning step was conducted using 2 keV Gallium (Ga) ion beam at an incident angle $<2°$ to the sample surface, minimizing the damage layer thickness. Hence, the Ga damage layer would be negligible compared to the thickness of the lift-out. The effect from this damaged layer would not significantly impact the TEM characterization results.

### *2.4. Characterization techniques (TEM/STEM, EDS, APT, microhardness)*

Dislocation loops were imaged in STEM bright-field (BF) mode using an FEI TF30 microscope. The dislocation loops were characterized using hand-counting techniques and the ImageJ software package to measure the dislocation loop diameter and number density from the STEM-BF images. The characterization of precipitate and matrix compositions was performed using the FEI Talos F200X scanning/transmission electron microscope (S/TEM) instrument equipped with high counting rate energy-dispersive x-ray spectroscopy (EDS) at the University of Michigan. The collected EDS signal was processed into weight/atom percentages for quantitative analysis using the Cliff-Lorimer method [29].

The atom probe tomography (APT) analysis was conducted at the Idaho National Laboratory (INL) using a Local Electrode Atom Probe (LEAP) system in a manner to minimize background noise for quantification of signals in the mass spectrum. The APT specimens from the proton irradiated Zr-4 sample were prepared by standard lift-out, and milling procedure using an FEI Quanta 3D FEG focused ion beam (FIB) instrument at INL. In this study, the typical APT needle specimen volume is $80 \times 80 \times 200$ nm$^3$. Data acquisition was performed on a Cameca LEAP 4000X HR instrument.

Microhardness tests at room temperature were conducted on all the irradiated materials. A Vickers Hardness indenter (Buehler MICROMET® II Hardness Tester) was employed to measure the post-irradiation microhardness at a load of 50 g, using 30 indentations per measurement. Measurements were made at the center of the irradiated area of the sample, with the indenter pushing into the outer irradiated face of the samples. The indent is about $20 \times 20$ μm$^2$ in size and penetrates about 2.8 μm. Accounting for a sampling depth that is ~3 times the indent depth yields a depth of roughly 8.4 μm, which is well within the FIB lift-out depth for the microstructure characterization in TEM and APT, well away from the region near the Bragg peak where damage rises dramatically.

## 3. Results

The result section consists of the characterization of the as-received and proton irradiated samples consisting of SPP amorphization and damage microstructure. Within each section the isothermal irradiation results will be presented first, followed by the two-step irradiation results.

### *3.1. As-received Zircaloy-4*

Detailed characterization of the base material before irradiation has been conducted. In summary, the microstructure and composition of the matrix as well as the C14 type hexagonal close-packed laves phase $Zr(Fe,Cr)_2$ SPPs were observed and agreed well with the early publications [24,25].

### *3.2. Proton irradiation*

#### *3.2.1. Amorphization of SPPs*

Isothermal proton irradiations were conducted to doses of 0.5, 1.6, and 5 dpa at five irradiation temperatures (250 °C, 280 °C, 310 °C, 330 °C, and 350 °C) to investigate total damage and irradiation temperature effects on laves phase SPP amorphization. Across the range of temperatures, only partial amorphization of the SPPs was achieved. An amorphous rim is observed to develop at the interface between the matrix and the $Zr(Fe,Cr)_2$ precipitates implying the transformation starts at the SPP perimeter and moves inward towards the center. As shown in Fig. 3 for samples irradiated at 280 °C, the amorphous rim thickens as the damage level increases. Amorphous rim thickness measurements at all the irradiation temperatures, as a function of dose and temperature, are graphically summarized in Fig. 4. A general trend for increasing amorphous rim thickness with increasing proton irradiation dose and decreasing irradiation temperature is observed. A typical damage layer by Ga beam from FIB sample preparation is parallel to the transmitted electron beam. Thus the amorphous rims depicted in Fig. 3 are actual amorphization rims formed by proton irradiation rather than artifacts from the FIB milling.

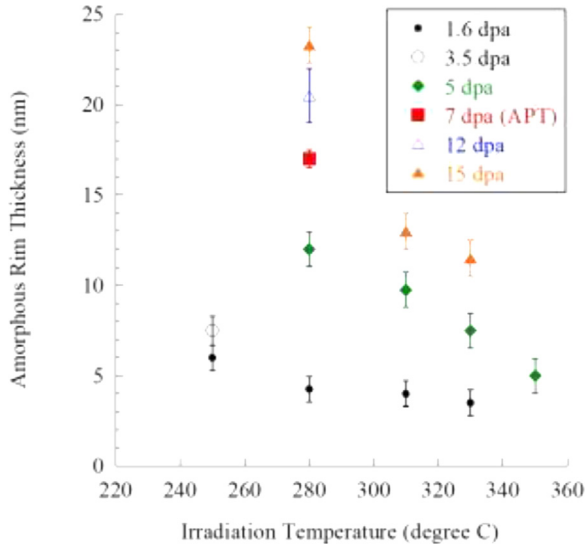


**Fig. 4.** Amorphization rim thickness was determined by STEM/TEM and APT (280 °C, 7 dpa sample) as a function of irradiation temperature and damage level. The 1.6 and 5 dpa samples were obtained from a depth of 3–5 $\mu$m below the irradiated surface, while the 3.5 and 12 dpa samples were obtained at a depth of 20–25 $\mu$m on a 1.6 dpa and 5 dpa sample, respectively. The 15 dpa samples were obtained at a depth of 23–27 µm beneath the irradiation surface. (Error bars represent ranges observed in SPPs measured under the given irradiation conditions. Typically, at least 5 precipitates per condition were analyzed.)

In Fig. 5, a comparison between non-irradiated SPP and low-temperature (-10 °C) proton irradiated SPP are shown. Fig. 5a shows a bright-field TEM image of the non-irradiated SPP, with staking faults (Fig. 5b also confirms its crystalline nature), which are often observed in the C14 Laves phase [25,26]. Fig. 5c shows EDS line profiles for a non-irradiated SPP that exhibits uniform Fe and Cr distribution (at the resolution of the EDS technique). The alloying element composition of the SPP is at ~ 45 at.% Fe and ~ 19 at.% Cr, which equates to a Fe/Cr (at/%) ratio of ~ 2.3, agreeing well with the reported value of ~2 ± 0.56 in the non-irradiated condition [25,30].

Following the first step of the two-step proton irradiation (-10 °C, to 2.5 dpa), the SPPs were observed to be completely amorphized, as indicated by the ring diffraction pattern shown in Fig. 5e. In Fig. 5f, the EDS analysis shows no outward diffusion of alloying elements from the SPP into the matrix, and Fe and Cr concentrations observed within the amorphized SPPs agreed well with the non-irradiated case in Fig. 5c, even at 2.5 dpa over 145 h of irradiation time. TEM analysis was performed after each step of the two-step irradiations. The amorphous state of the SPPs was preserved following the second step of 2.5 dpa at 350 °C.

### 3.2.2. Fe loss from SPPs

All elevated temperature, isothermal irradiation conditions produce insignificant amorphization rims on the order of 10–20 nm, shown in Fig. 3. It is important to note that, due to the very thin dimensions of the amorphous rim regions of the precipitates in the isothermal proton irradiated samples, the majority of the SPP remains as crystalline, and the composition remained near the original composition of the SPP. Hence, only the first 100 nm of SPP at the matrix/SPP interface was analyzed for any chemical composition changes, as illustrated in Fig. 6 (a,b). EDS analysis was only carried out on SPPs that contain an edge-on section through the thickness of the lift-out, and the SPP/matrix interface was tilted parallel to the electron beam to minimize any overlapping effects from the matrix. All EDS maps were collected on the same instrument with identical parameters. The raw data obtained on the percentage of alloying element (i.e., Fe+Cr) loss was also corrected against non-irradiated SPP references for a more accurate assessment.

In Fig. 6(c), at a damage level of 5 dpa, the Fe+Cr loss peaks at 330 °C for the isothermal irradiations with a mean value of ~14% depletion, whereas the two-step irradiation sequence achieved a ~29% depletion. It should be noted, alloying element depletion shown in Fig. 6(c) fails to correlate with the amorphization behavior observed in Fig. 4. As the irradiation temperature increased from 280 to 330 °C, there was an increase in alloying element de-

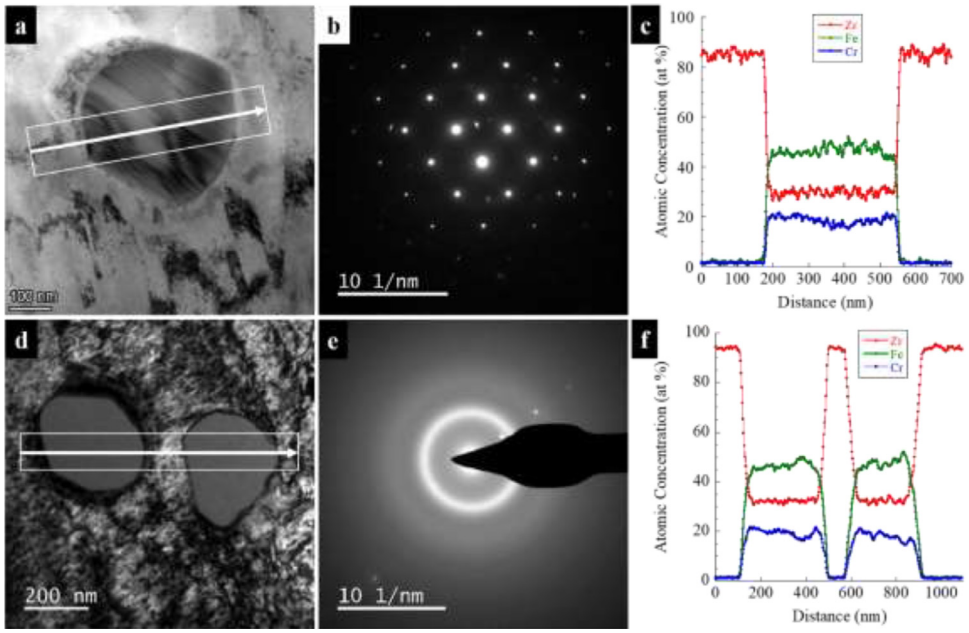


**Fig. 5.** Comparison between (a) non-irradiated $Zr(Fe,Cr)_2$ SPP and (d) proton irradiated SPP at -10 °C up to 2.5 dpa of damage. The selected area electron diffraction (SAED) obtained from the SPPs shows (b) a crystalline nature of the non-irradiated SPP, while (e) a ring pattern was obtained for the low-temperature irradiated SPP, indicating its amorphous nature. Both EDS line profiles (as indicated by white arrows in the TEM images) are shown in (c) and (f) are consistent in alloying elements concentration, indicating the lack of alloying element redistribution through the low-temperature irradiation step.

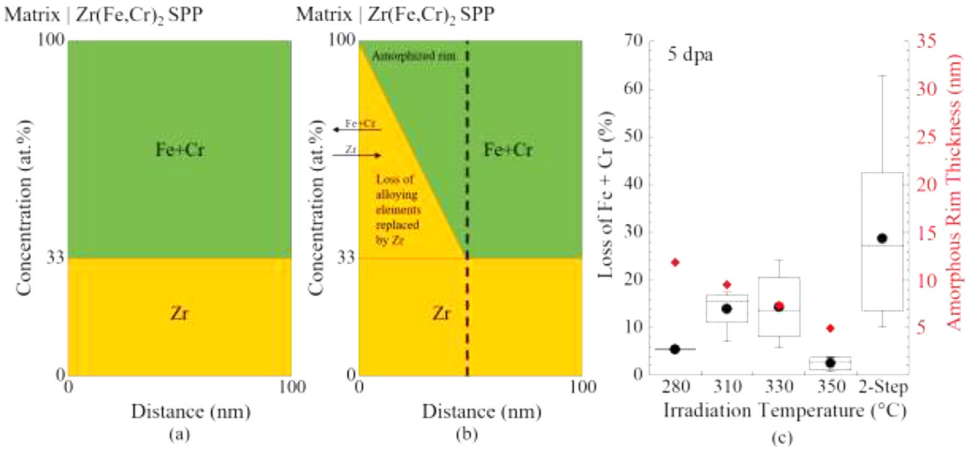


**Fig. 6.** Schematic of the alloying element loss analysis from EDS line profile across an SPP, (a) non-irradiated SPP composition profile in the first 100 nm, (b) composition profile of the SPP after proton irradiation, (c) correlation between the percentage of (Fe+Cr) loss and amorphization layer thickness as a function of irradiation temperatures and methods (i.e., isothermal or two-step irradiations).

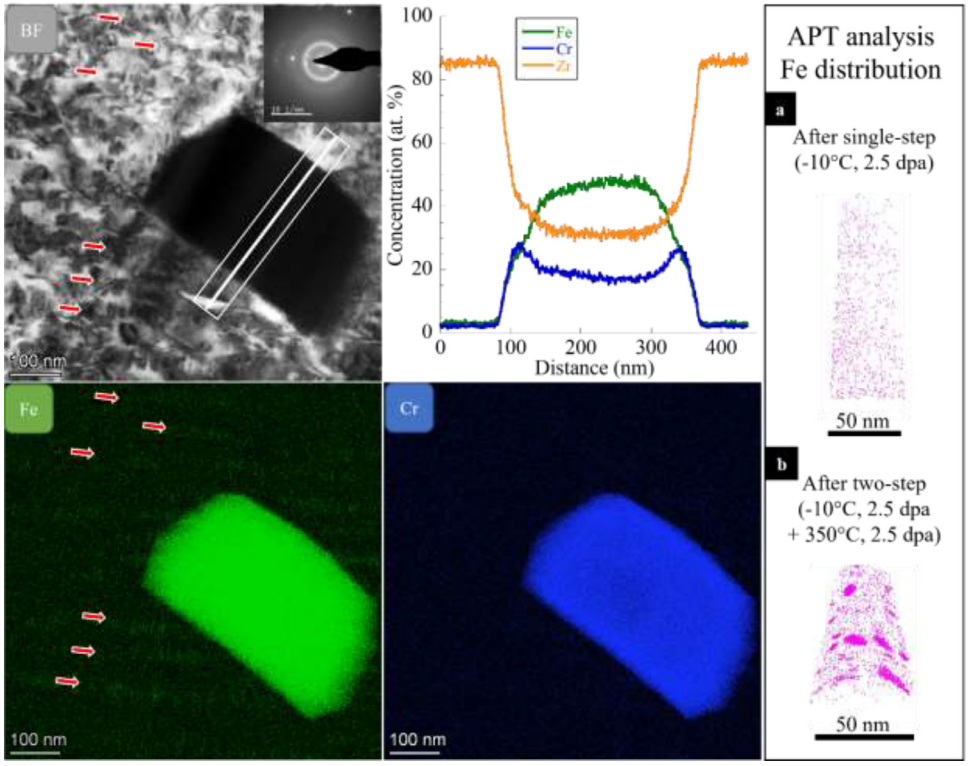


**Fig. 7.** Bright-field STEM image and EDS maps of laves SPP after a two-step proton irradiation sequence. The diffraction pattern of the entire precipitate with a ring reflection shows the amorphous nature of the SPP. EDS maps of SPP revealed its core-shell structure with a Fe depleted shell. EDS line-scan profile indicates the chemical composition across the precipitate indicated by the white arrow in the bright-field image. Rafts are apparent in the BF-STEM image and Fe map, and their positions are indicated by the red arrows. Atom probe tomography volumetric reconstructions of the needles that were taken from (a) single-step liquid nitrogen cooled -10 °C proton irradiation to 2.5 dpa, no measurable Fe cluster was observed, and (b) same bar being irradiated again isothermally at 350 °C to an additional 2.5 dpa, multiple Fe clusters has been identified and overall Fe content of the needle is 0.08 at.%. (For interpretation of the references to color in this figure legend, the reader is referred to the web version of this article.)

pletion from the near interface region of the SPP, although amorphization rim thickness decreased at higher irradiation temperatures.

Following the two-step irradiation sequence, not only did the SPPs remain amorphous, they also exhibited Fe depletion on the periphery of the particle, Fig. 7. This depleted region appears to be on the order of ~50 nm, which is significantly thicker than that produced with isothermal proton irradiations to 5 dpa in the temperature range of 250–350 °C (Fig. 4). Iron and chromium levels in the center of the ~300 nm particle remain close to the non-irradiated case (e.g., at Zr ~ 33 at.%, Fe ~ 45 at.%, Cr ~ 20 at.%) shown in Fig. 5c for as-received material.

Due to the limited detection level of STEM-based EDS techniques, the matrix Fe content was determined using atom probe tomography. In Fig. 7a, after irradiating with protons to 2.5 dpa at -10 °C, the matrix Fe content is the same as the as-received material, with no visible Fe clusters or segregations. However, when the same sample was irradiated at 350 °C for an additional 2.5 dpa, a large number of Fe clusters had developed with an average cluster size of 5–10 nm, as shown in Fig. 7b. The overall matrix Fe concen-

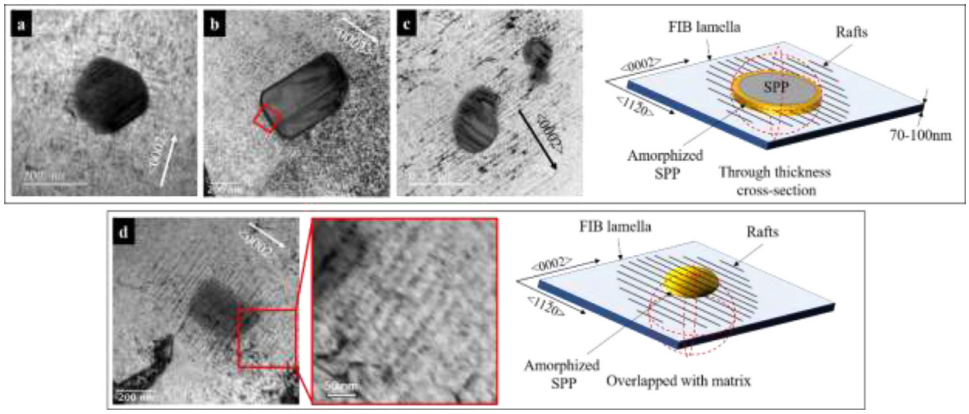


**Fig. 8.** Bright-field TEM images were taken from near a <11-20> zone axis, with two beam $g = 0002$ diffraction conditions. Fe-rich rafts are observed in the vicinity of SPPs in Zircaloy-4 that was proton irradiated at (a) 250 °C to 1.6 dpa, b) 280 °C to 5 dpa, c) 330 °C to 5 dpa (an EDS analysis of the highlighted region, marked in red, is shown in Fig. 9), via through-thickness cross-section (prepared through the center of the SPP, to represent the maximum amorphous region) FIB lamella preparation, where rafts are only observed in the nearby matrix; and (d) proton irradiated at 280 °C to 5 dpa where lamella containing an amorphous SPP with the overlapped matrix that contains rafts, and each raft can be seen as a stack of individual features arranged linearly.

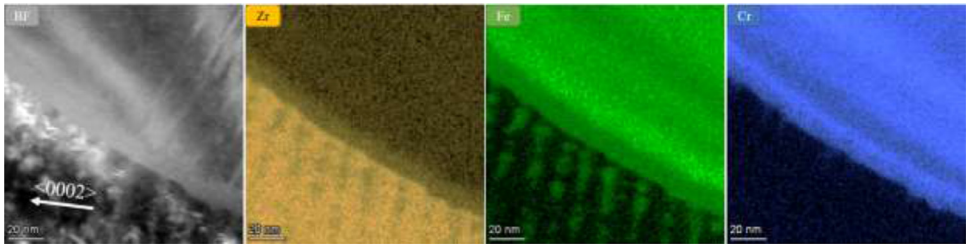


**Fig. 9.** Rafts were observed in a linear formation parallel to the basal planes next to a $Zr(Fe,Cr)_2$ precipitate irradiated with a proton beam at 280 °C to 5 dpa (top right). Dark-field STEM image of the region highlighted in Fig. 8b, and elemental maps of Zr, Fe, and Cr. (For interpretation of the references to color in this figure legend, the reader is referred to the web version of this article.)

tration after the two-step irradiation sequence rises from no measurable Fe level to ~ 0.08 at. %.

### 3.2.3. Raft formation near SPPs

Non-uniform distributions of rafts (the aligned interstitial loops in the matrix or close to SPPs where egress of Fe is the largest) of defects have been observed in the matrix near precipitates following neutron irradiation [1,16]. In Fig. 8, such "rafts" are typically observed in the vicinity of SPPs after proton irradiation. The 3D distribution of the rafts around an SPP can be visualized by the schematics shown in Fig. 8, where the rafts appear to originate from the SPPs and extend 150–200 nm into the matrix. In Fig. 8 (a–c), the rafts are observed as early as 1.6 dpa at an isothermal irradiation temperature of 250°C. However, as isothermal irradiation temperature increased to 280–330 °C, the rafts were not observed until the damage reached ~5 dpa. Raft formation was not observed after isothermal irradiation at 350 °C, even at 5 dpa. The magnified image shown in Fig. 8d, indicates that these rafts consist of individual nano-sized features clustered linearly. The planes on which these rafts reside coincide with the basal planes. The image was taken from the <11–20> zone axis, with the beam parallel to the $g = 0002$ systematic row. The spacing between the rafts is 15 and 20 nm. Idrees et al. also observed <a>-component loops after heavy ion irradiation, arranged along the trace of the basal plane in rafts, with ~ 20 nm spacing between the rafts [31]. Raft formation was also observed after the two-step irradiation sequence, Fig. 9, with a width of ~10 nm, similar to the literature value for <a> loops observed in neutron irradiated materials.

Detailed elemental maps shown in Fig. 9 indicate these rafts are enriched with Fe and some traces of Cr. The Fe map also reveals the same nano-sized features in these rafts in Fig. 9. Clustering of alloying elements to these planar features has also been observed in neutron and proton irradiated Zircaloy-2, where Fe and Cr segregation leads to clustering or precipitation around SPPs [32,33]. In Fig. 7, similar linear features were observed near the SPP in the matrix in the two-step irradiation sequence.

### 3.2.4. Dislocation loops

A representative STEM bright-field image of loops observed in proton irradiated Zircaloy-4 after isothermal irradiation, Fig. 10a, shows the light and dark band contrast caused by <a> loop clustering in a linear configuration. Loop sizes of 15–25 nm are observed in the 330 °C and 350 °C isothermal irradiated samples at doses >2.5 dpa.

Fig. 10b shows <c> loops observed in the same sample as Fig. 10a, at a slightly different orientation. The electron beam was parallel to the basal plane in Fig. 10b. Since the <c> loops form on the (0001) basal planes with <c> component Burger vectors, the <c> loops are observed edge-on as projected line segments. The <c> loop densities were estimated at $3.34 \times 10^{20} m^{-3}$ for the 2.5 dpa 350 °C sample and $8 \times 10^{20} m^{-3}$ for the 5 dpa 330 °C. The average size of the <c>-loop is typically 150 nm.

Upon completing the two-step irradiation sequence, <a>-loops are visible in Fig. 11a, where the alternating light and dark band contrasts caused by <a> loop clustering and alignment is also seen. The <a>-loop clustering and alignment has been reported numerous times and is a banding of purely <a>-loop parallel to the trace of the basal plane [34–36]. Northwood et al. also reported that the <a>-loop alignment was consistently seen in neutron irradiated Zircaloy-2 and definitively concluded that it was not caused by <c>-component damage or as an artifact [34]. The <a>-loop density in Fig. 11b is estimated to be approximately $5.3 \times 10^{21} m^{-3}$, similar to the results obtained on proton irradiated Zircaloy-2 by Harte et al. [32]. Fig. 11b indicates the <a> loop sizes are on the

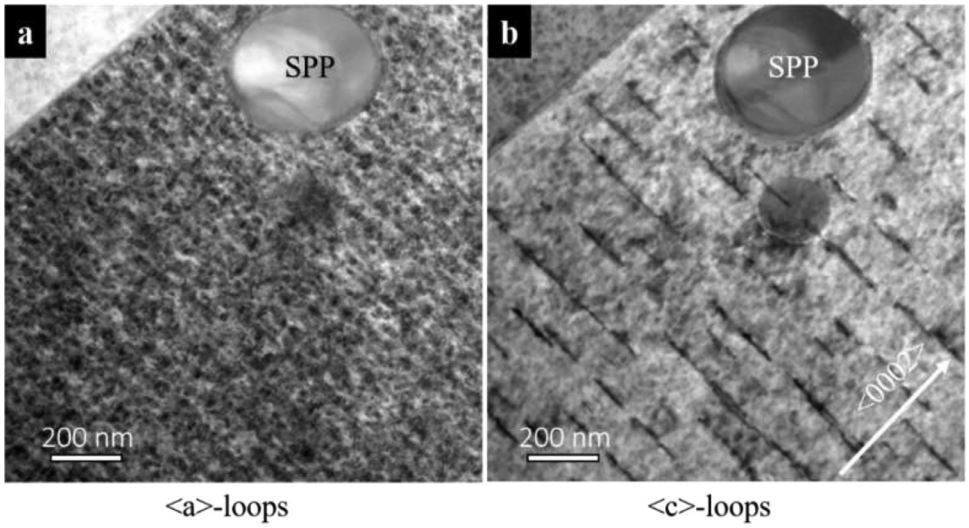


**Fig. 10.** STEM bright-field image of loops observed on proton irradiated Zircaloy-4, both images were taken from the exact location on the lamella, with two different tilts, (a) <a> loop formation showing <a>-loop alignment after 2.5 dpa at 350 °C, (b) <c> loops edge-on in two-beam $g = 0002$ diffraction condition appears as dark line segments after 2.5 dpa at 350 °C.

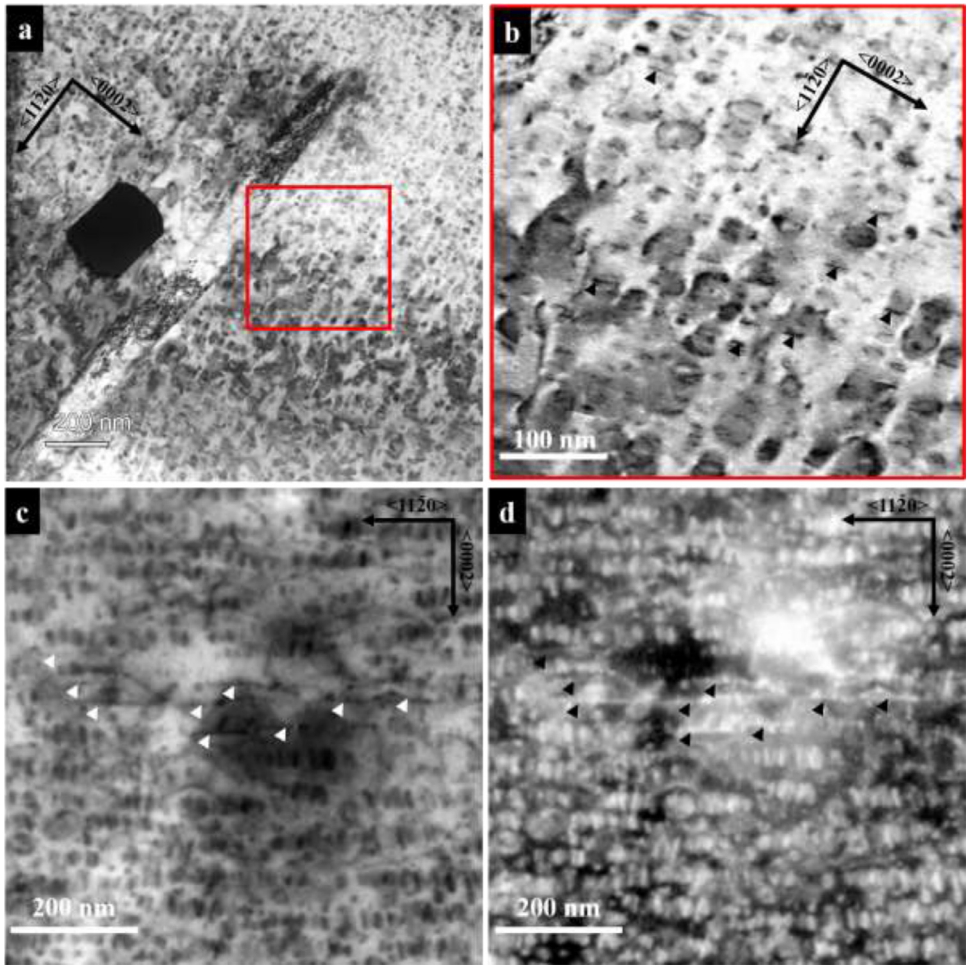


**Fig. 11.** STEM images of loops observed after the two-step proton irradiated Zircaloy-4, (a) bright-field image of <a>-loop alignment, and (b) zoomed-in image of the area of interest showing in Fig. 11a with some of the edge-on <a> loops (indicated by the black arrows) appearing as line features, (c) and (d) are <a> and <c> loops (<c>-loops are indicated by arrows) imaged under two-beam $g = 0002$ diffraction conditions near the <11-20> zone axis.

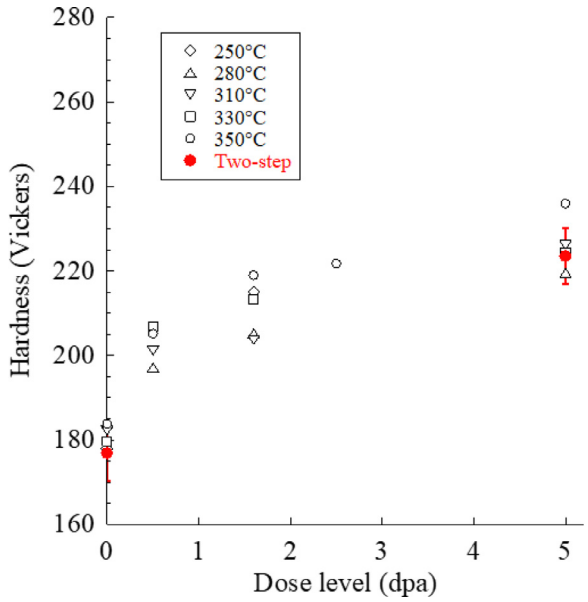


**Fig. 12.** Dependence of the Vickers microhardness number on irradiation dose level (dpa) and irradiation temperature on isothermal and two-step proton irradiated Zircaloy-4.

order of 25 ± 9 nm. In projection, some of the <a> loops appear to be parallel with the beam, showing as line features as indicated by the black arrows in Fig. 11b. Loops on the other prism planes appear to be elliptical with a darker contrast. Figs. 11c and 14d are STEM images taken under $g$ = <0002> two-beam imaging conditions illustrating <c>-loops are also observed in the two-step irradiated sample, with a size of 100–150 nm. The arrows indicate where the <c>-loops were located, and it should be noticed that <a>-loops were absent where <c>-loops were present, which has also been reported by Harte et al. [32] on proton irradiated Zircaloy-2.

### 3.2.5. Irradiation hardening

Vickers microhardness data from proton irradiated samples obtained for each irradiation condition are plotted in Fig. 12. The hardness data indicates that microhardness increases rapidly with increasing proton dose in the low damage range and tapers off above 1, 2 dpa, matching other published results obtained on proton irradiated Zircaloy-4 at similar irradiation temperature and doses [18]. Interestingly, a general trend is observed in Fig. 12 for an increased hardness at any given dose, with increased irradiation temperature. This is opposite the trend under neutron irradiation [37].

The hardness values following the two-step irradiation fell between those obtained from 280 °C to 350 °C isothermal irradiations, Fig. 12. The slightly increased hardness compared to the lower bound 280 °C irradiation may be contributed by the Fe cluster formation observed earlier in Fig. 7b, during the second half of the irradiation. These solute-rich clusters could develop into precipitates and act as obstacles for dislocation motion, resulting in a hardness increase.

## 4. Discussion

This section will compare the microstructures of the SPP and matrix of the proton irradiated samples, such as SPP amorphization, Fe redistribution, and irradiation hardening, to microstructure observations from the neutron irradiated samples.

### 4.1. Amorphization of SPPs

At LWR operating temperatures (270–350 °C), the SPPs typically evolve under neutron irradiation in two ways, amorphization (occurring in the lower temperature range and starting at damage levels of only a few dpa) and dissolution (occurring only after very high damage levels at all temperatures). This discussion will address the extent of SPP amorphization as a function of irradiation damage and Fe and Cr loss from the amorphized SPP and its redistribution into the matrix.

Laves phase SPP amorphization under neutron irradiation at LWR operating temperatures typically starts at the outer surface of the SPP and progresses inwards with increasing fluence. It has been reported by Etoh and Shimada [38], where the partially amorphized SPP consists of a crystalline core surrounded by an amorphous rim layer. As neutron fluence increases, a complete amorphization of the SPP can be achieved. In the current study, isothermal proton irradiation, even at high damage levels (~15 dpa) at the LWR operating temperatures (280–350 °C), has only resulted in partial amorphization of the SPPs, with only a small fraction of the precipitate amorphized. Conversely, as Kammenzind et al. indicated, at comparable damage levels under neutron irradiation (13 dpa, or 9 × $10^{21}$ n/cm$^2$, E> 1 MeV) amorphous rims extending ~100 nm into the SPP are observed.

Griffiths et al. [39,40] and Gilbon and Simonot [41] determined that the amorphization process under neutron irradiation is proceeding at a rate of ~ 10–13 nm per $10^{25}$ n/m$^2$, $E$ > 1 MeV (~ 1.45 dpa), which is ~ 7–9 nm per dpa. Motta [42] and Bajaj et al. [24] also support this amorphization rate in neutron-irradiated $Zr(Fe,Cr)_2$ precipitates. Bajaj shows an even higher amorphization rate is possible in the lower end of the LWR operating temperature range of ~ 260 °C. The isothermal proton irradiations in this study are producing amorphous rims in the second phase $Zr(Fe,Cr)_2$ SPPs at a rate of ~ 3, 4 nm per dpa or less (for the 1.6 dpa samples), which is less than one-half of the rate occurring under neutron irradiation.

The compendium of information produced in this study using proton irradiation temperatures ranging from 250 °C to 350 °C shows that amorphization of laves SPPs in Zircaloy-4 occurs more slowly as a function of dpa than does neutron irradiation. The amorphization rate from both neutron and proton irradiations is shown in Fig. 13a as a function of the damage rate. In general, damage rates under proton irradiations are at least two orders of magnitude higher than under LWR neutron irradiation conditions. However, the data suggests that amorphization rates as a function of dpa under neutron irradiation are higher than under proton irradiation. The slower amorphization rate as a function of dpa occurring under proton irradiation is a factor of 2, 3 lower than the bulk of the neutron irradiation data, despite the two orders of magnitude higher damage rate as a function of time.

The irradiation temperature also has a pronounced effect on the amorphization fraction of the SPP, as shown in Fig. 13b, in which the amorphization rate decreases with increasing temperature for both neutron and proton irradiations. The amorphous rate of SPP follows a roughly linear relationship with a negative slope as a function of irradiation temperature, as shown in Fig. 4. Irradiation-induced SPP amorphization is expected to show an inverse irradiation temperature dependence since the higher temperature will increase the tendency of back-diffusion, impeding the radiation-induced redistribution of alloying elements or amorphization of the crystalline phase. The same observations from both neutron and proton irradiations are further supported by the irradiation-induced amorphization model developed by Wang et al. [44], which assumes that amorphization is related to a crystallization efficiency parameter $A$. For low values of $A$, as would be expected for low irradiation temperatures, the accumulation of the

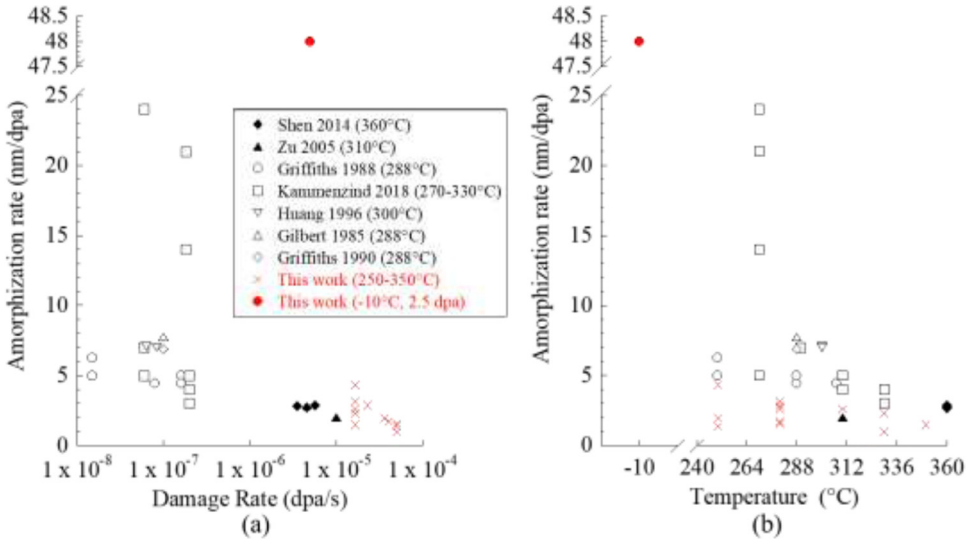


**Fig. 13.** The amorphization rate of $Zr(Fe,Cr)_2$ SPPs as (a) a function of damage rate; (b) a function of irradiation temperatures. Neutron irradiation data are shown as open symbols, and proton irradiation data are shown as solid symbols. Neutron fluence data were converted using an average value of $0.6 \times 10^{25}$ n/m$^2$ per dpa [43].

amorphous fraction as a function of the dose is an exponentially increasing function. As irradiation temperature decreases, the dose for amorphization also decreases exponentially. This was shown by the two-step irradiation in which the SPPs were completely amorphized after 2.5 dpa at -10 °C. Data from Griffiths et al. [39] suggests that critical amorphization temperature ($T_{c-a}$) for laves phase precipitates in Zircaloy under neutron irradiation in an LWR environment is above 80 °C, and maybe approaching 280 °C under high neutron flux conditions. The two-step proton irradiation performed in this study suggests that $T_{c-a}$ for laves phase precipitates under proton irradiation should be somewhere between Tc-a of neutron and electron (which is close to room temperature). The fact that amorphization is observed uniformly at -10 °C on the laves phase indicates that the irradiation temperature (-10 °C) is well below the $T_{c-a}$ for proton irradiation.

The data in Fig. 4 shows that as irradiation temperature increases, all the datasets for different damage levels appear to converge to a "non-amorphization" point at about 380–400 °C, where the current proton irradiation conditions would likely be insufficient to amorphize the $Zr(Fe,Cr)_2$ SPPs. This upper-bound temperature limit inferred from the proton irradiation data is slightly higher than the upper-bound temperature reported in [45] for neutron irradiation, which is at ~ 330 °C, but is likely still higher based on the 330 °C data in [24]. In typical commercial power reactors, the thermal energy below ~330°C is insufficient to maintain long-range order in the hcp $Zr(Fe,Cr)_2$ precipitates, and these intermetallic SPPs gradually become amorphized. In this proton irradiation study, it appears thermal energies above 380–400 °C may be required in order to maintain long-range order at the dpa rates used in this study. The required higher temperature under proton irradiation inferred in this study may result from the two orders of magnitude greater damage rate occurring under the proton irradiation conditions used, as illustrated in Fig. 13a.

Another factor that influences amorphization is the cascade size caused by the irradiating particle, which relates to the local density of the defects. The cascades created by neutron irradiation and proton irradiation are very different in morphology and size, with cascades caused by neutron irradiation being much larger and denser. As illustrated by Was and Allen, in Ref. [45], neutrons produce the largest cascade size, similar to heavy ions, with protons producing significantly smaller cascades. The effect of cascade size was established in this study by irradiations conducted at the same temperature and damage rate as the proton irradiations, but using self (Zr) ions. The Zr self-ions completely amorphized the SPPs in Zircaloy-4 by 1.6 dpa at 250 °C. (to be included in a forthcoming paper).

### 4.2. Alloying elements redistribution

The diffusion of Fe in Zr is by an interstitial diffusion mechanism, yielding a Fe diffusion rate that is several orders of magnitude faster than Zr self-diffusion [46]. The amorphization of $Zr(Fe,Cr)_2$ precipitates under neutron irradiation at LWR operating temperature is always accompanied by Fe depletion in the amorphous region [42]. Topping et al. and Sundell et al. both reported that Fe clustering was observed throughout the matrix in proton-irradiated Zr-0.1Fe and neutron irradiated Zircaloy-2 [47,48]. Francis et al. [15] have also observed Fe depletion from the Zr(Nb,Fe,Cr) SPPs during proton irradiation, starting from the periphery of the particle. This observation has been confirmed under both isothermal proton irradiation (Fig. 9) and two-step proton irradiation (Fig. 7) in this study, where Fe content dropped from ~45 at.% (original SPP Fe level) to ~25 at.%. There is significantly more Fe remaining in the core region (amorphized or crystalline) of the irradiated SPP, than in the Fe depleted amorphous rim, in agreement with neutron irradiated SPPs observed in Ref. [24]. As illustrated in Fig. 6, the loss of alloying elements peaked at 330 °C under isothermal irradiation conditions. There is likely to be a threshold temperature for alloying element depletion between 330 and 350 °C, where amorphization and depletion of Fe become difficult due to the elevated thermal energy and the favorable condition to maintain long-range ordering in a crystal. The changing composition of the precipitates under irradiation is likely enhanced by the greater mobility of Fe than Cr in the surrounding Zr matrix under irradiation. However, this Fe depletion was only observed when irradiation temperature is high enough for sufficient Fe mobility. The experiment conducted at -10 °C to 2.5 dpa, where no Fe was detected in the matrix (Fig. 5f), demonstrated that even with full amorphization of the SPP, Fe redistribution would not occur due to the insufficient thermal diffusion of Fe. It implies that amorphization is necessary but not sufficient to distribute Fe away from the $Zr(Fe,Cr)_2$ precipitates; thermal diffusion and irradiation enhanced mobility of Fe must also be acting synergistically. Hence, the sec-

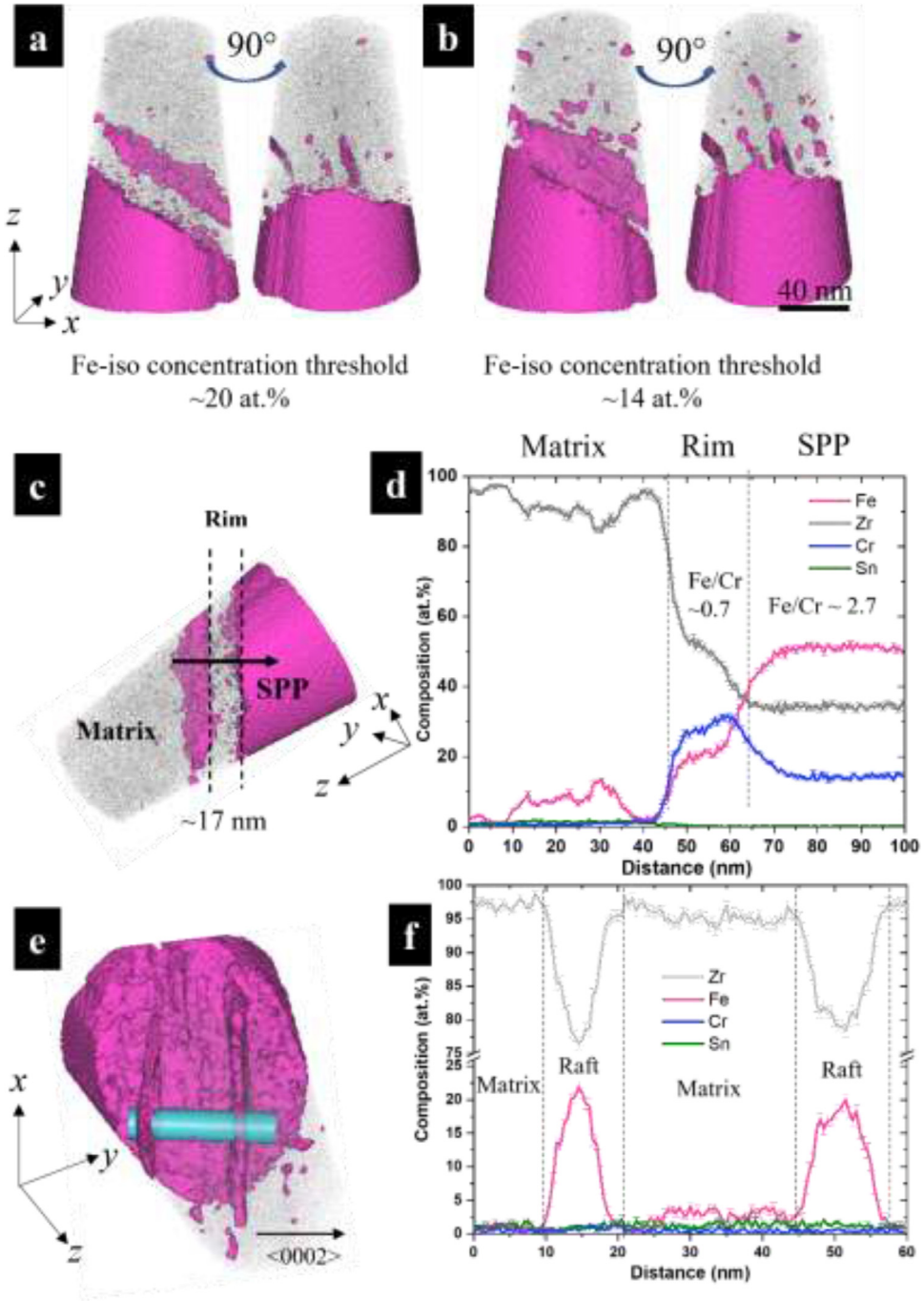


**Fig. 14.** The APT measurement was taken at an SPP/matrix interface from Zircaloy-4 that was proton irradiated at 280 °C to 7 dpa, a) reconstructed volume using an iso concentration surface threshold of 20 at.% Fe showed in magenta and Zr in gray, and (b) reconstructed volume using a 14 at.% Fe iso-concentration threshold, (c) the reconstructed volume was oriented to show the matrix/SPP interface, (d) composition profile of the arrow line shown in (c), (e) reconstructed volume was oriented to show rafts that are edge-on and parallel with the basal plane, and (f) the chemical profile across two rafts shows in (e).

ond part, high-temperature irradiation of the two-step approach, was designed primarily to enhance Fe redistribution.

The redistribution of Fe from the amorphous part of the SPP to the matrix is a diffusional process with irradiation enhancement, i.e., increased defect concentrations and dislocation loop structure. Determination of volumetric matrix Fe content via APT has been conducted in this study. However, due to the non-uniform redistribution of Fe from the amorphized SPP into the matrix, the APT measurement results were largely dependent on proximity to SPPs, hence resulting in a large scatter of the data. On the contrary, the SPP iron loss measurements at 5 dpa summarized in Fig. 6, offer a meaningful representation of the total alloying element redistribution from a sourcing standpoint.

The APT technique is a powerful tool to capture the interfacial details between SPP and matrix, due to the high spatial resolution and volumetric visualization. For the case of irradiation at 280 °C to 7 dpa shown in Fig. 14 (a, b), the APT needle captured the various interfaces between an SPP and the matrix. By adjusting the iso-concentration threshold for Fe, the amorphous rim on the SPP surface was shown to have a considerably lower Fe concentration compared to the SPP bulk composition. Moreover, the platelet features in Fig. 14 (a, b) extending out of the amorphous rim into

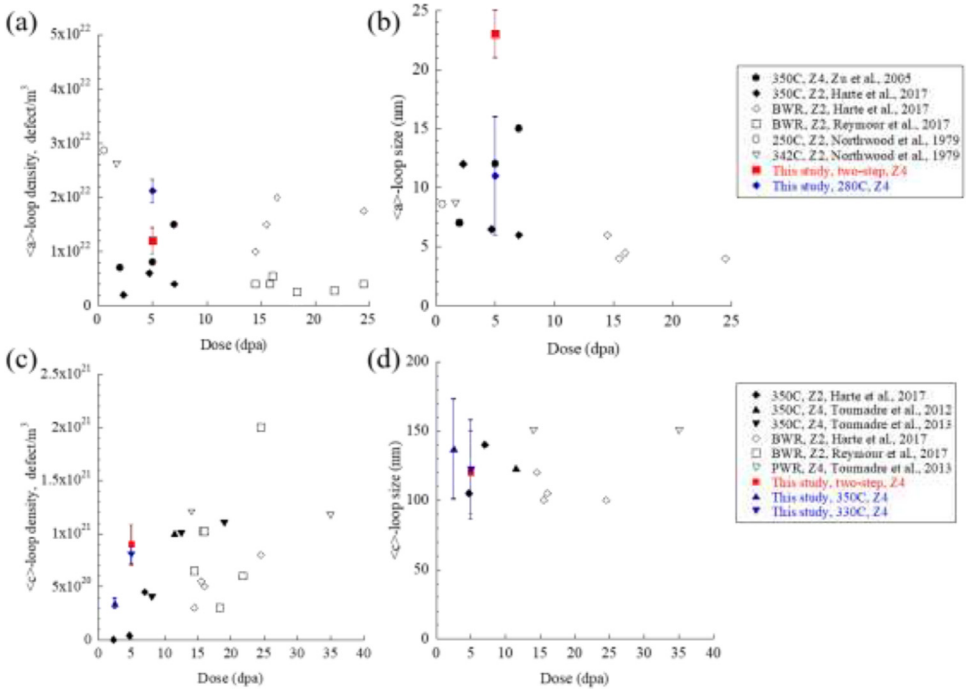


**Fig. 15.** Comparison of dislocation loop density and size. In (a) and (b), the <a>-loop volumetric density and size with irradiation dose are plotted against data from other proton (solid symbols) or neutron-irradiated results (open symbols). The <c>-loop density and size as a function of dose are plotted in (c) and (d). The dimension of the <c>-loop in (d) are the measurements of the projected length of <c>-loops in a direction parallel to the $g = 0002$ systematic row. A conversion factor of $0.6 \times 10^{25}$ n/m$^2$ per dpa was used for converting the neutron fluence to dpa [43].

the matrix share many features in common with the rafts observed around the SPP by TEM in Fig. 8. In Fig. 14c, where the amorphous rim is orientated such that the rim is edge-on, the thickness of the rim is 17 nm. The chemical composition across the matrix/SPP interface is shown in Fig. 14d, where the Fe concentration in the amorphous rim shows a plateau at ~ 20 at. %. The bulk SPP Fe concentration is consistent with the EDS data collected on a non-irradiated SPP shown in Fig. 5c, at ~ 45–50 at.%. The Fe/Cr ratio in the amorphous region is at ~ 0.7, which is significantly lower than the value measured for the crystalline core of the SPP at ~ 2.7 (this is within the range of Fe/Cr ratio 1–3.25, reported by Anderson and Bajaj, on the Laves phase precipitates in $\alpha$-annealed Zircaloy-4 [25]). In Fig. 14e, the reconstructed volume is orientated such that the "rafts" are edge-on. The chemical profile across these rafts is illustrated in Fig. 14f along the cylindrical volume indicated in Fig. 14e, with an average of 17 at. % Fe in the raft. The typical thickness of these rafts is 7–10 nm, consistent with the <a>-loop sizes observed in both proton and neutron irradiated materials. It must also be noted that APT has confirmed both the presence and dimension of Fe clusters in the matrix near the SPP, which may also aid the interpretation of rafting formation observed in Fig. 9.

### 4.3. Dislocation loops

#### 4.3.1. Loop sizes and densities

Topping et al. also reported that <a>-loops vary in size with irradiation temperature in proton-irradiated Zr alloys [17]. While it is challenging to identify whether a particular loop is interstitial or vacancy in character, there is general agreement that a higher fraction of <a> loops are interstitial at irradiation temperatures below approximately 300 °C and a higher fraction are vacancy loops at irradiation temperatures above approximately 400 °C [49].

Past proton irradiation studies at irradiation temperatures of 350 °C appear to reasonably emulate <a> loop formation in Zircaloy-4 [18,32]. Fig. 15(a, b) show the <a>-loop number density and size obtained from the current study plotted alongside literature data published previously on proton and neutron irradiated Zircaloys. Typical <a>-loop diameters of 7–22 nm and number density ranging from $5 \times 10^{20}$to $5 \times 10^{22}$ defect/m$^3$, are reported in many publications [34,35], with irradiation temperature close to 350 °C and neutrons fluence above $1 \times 10^{25}$ n/m$^2$. At temperatures of 300 °C or below, loop diameter ranges between 5 and 50 nm [35], and a higher loop number density has been observed. This was indeed observed on the isothermal proton irradiation data at 280 °C (5 dpa) in Fig. 15a, where <a>-loop density was slightly higher than other proton irradiation data, while still in good agreement with the neutron irradiation data. The <a>-loop number density of the two-step irradiation conducted in this study agrees well with other proton irradiations at 350 °C, while it is slightly lower than the neutron data at a lower dose level and at lower irradiation temperatures [34]. With increasing neutron irradiation temperature, <a> loop diameter increases, and loop number density decreases [34,36,50]. Thus, the two-step proton irradiation reasonably reproduces the <a>-loop microstructure in Zircaloy-4 as it would be expected from neutron irradiations.

At higher irradiation damage conditions of ~5 dpa (or ~$3 \times 10^{25}$ n/m$^2$) or more under neutron irradiation, depending upon the irradiation temperature, <c>-loops begin to form on the basal plane. <c> component loops tend to be significantly larger than the <a>component loops, with a density that continues to increase as irradiation dose increases [35,51]. Tournadre et al. [52] showed that <c> component loops emerged under proton irradiation at a dose similar to that in the reactor case. In this proton irradiation study, <c>-loops are commonly observed in high dose level samples irradiated at temperatures of 330 °C and 350 °C. (No <c> loops were observed through 5 dpa at the lower irradiation temperatures.) The <c>-loop sizes and the loop densities are in the range of that observed under neutron irradiation, as illustrated in Fig. 15 (c, d). In summary, both the <a>- and <c>-loops have been observed in our isothermal and two-

step proton irradiations, and the sizes and number densities of the loops are consistent with the neutron and other proton irradiation data available in the literature. The fact that <c> loop formation in this study is only observed after high dose irradiations at temperatures of 330 °C and 350 °C may be a further indication that the matrix iron content is greatest following high dose proton irradiations at the higher temperatures of 330 °C to 350 °C. Matrix iron concentration has been identified as one factor potentially stabilizing <c> loop formation [53].

#### 4.3.2. Alignment of <a>-loops

The <a>-loop alignment is observed after neutron irradiation, where <a> loops are aligned in rows or layers along the trace of the basal plane with the appearance of light and dark bands contrast [54]. Interstitial and vacancy loops are located in alternate rows in these light and dark bands, explaining why the two types of loops can co-exist in the irradiated microstructure. Our observations, shown in Fig. 8 (a–c) and Fig. 11, confirm that proton irradiation at similar damage levels and irradiation temperatures can produce such microstructural features analogous to neutron irradiation.

Fe-rich features appearing as rafts every few dozen nanometers were observed in the EDS and APT analysis shown in Figs. 7, 9, and 14. Since Fe solubility in $\alpha$-zirconium is extremely low, 0.006 -0.03 wt. % [47,50,55,56], most alloyed Fe will be in the form of SPPs in the as-manufactured, non-irradiated material. Fe clustering in the matrix will be very difficult unless a large concentration of Fe is dissolved into the matrix. Significant <a>-loop formation occurs in zirconium at lower damage levels than significant Fe redistribution out of the laves phase particles [35]. Thus, ordered Fe-rich clustering has not been generally observed in the matrix of proton irradiated Zr by TEM, except for areas in the SPP vicinity [16,32]. The formation of Fe-rich rafts near SPPs was observed throughout the isothermal proton irradiation conditions in this study, even at a temperature as low as 250 °C to a damage level as low as 1.6 dpa, with SPPs being only minimally amorphized (as shown in Fig. 8a).

This localized Fe redistribution has also been reported in other studies of zirconium alloys that were subjected to neutron irradiations. Kammenzind et al. [1] and Holt & Gilbert [57] observed raft formation near SPPs in Zircaloy-4 at 300 °C after neutron fluence of $8 \times 10^{25}$ n/m$^2$ (~13.3 dpa). Sawabe et al. [58] observed Fe and Cr rich clusters to periodically appear near the SPP after six cycles in a BWR at 283 °C. The spacing between these rafts in the neutron-irradiated Zircaloy-2 was ~ 23 nm, which is in good agreement with the current proton irradiation study on Zircaloy-4 shown in Fig. 8d. It is speculated that if <a> loops form before Fe segregates to them, then the loops in the rafts should be at a similar size compared to the loop size found in the matrix, as observed. From TEM analysis in Fig. 7, the <a> loops in the matrix, being ~ 10 nm in diameter, are of the same size compared to the Fe-rich rafts near the SPPs, as shown in Fig. 14f.

From our APT results, there are mixed observations on Fe cluster formation in the matrix. A spectrum of results was observed, ranging from no cluster formation (e.g., the detection limit for Fe in some APT tips) to a large concentration of Fe clusters found in the matrix with cases of periodic clustering of Fe-rich features (e.g., APT reconstructed volume shown in Fig. 7b). This is evidence for the proposed mechanism that Fe found in the form of clusters was supplied by nearby amorphized SPPs, and the density of these Fe clusters would follow a diffusion gradient away from the SPPs. Indeed, this would explain the observation of rafts only found near an SPPs in TEM analysis. Significant Fe redistribution and formation of Fe-rich clustering throughout the matrix after proton irradiation has been reported on Zircaloy-2 with 60 nm size SPPs [40]. The more homogeneous Fe redistribution may have resulted from the smaller SPP sizes of the Zircaloy-2, which are more susceptible to amorphization and dissolution at any given damage level.

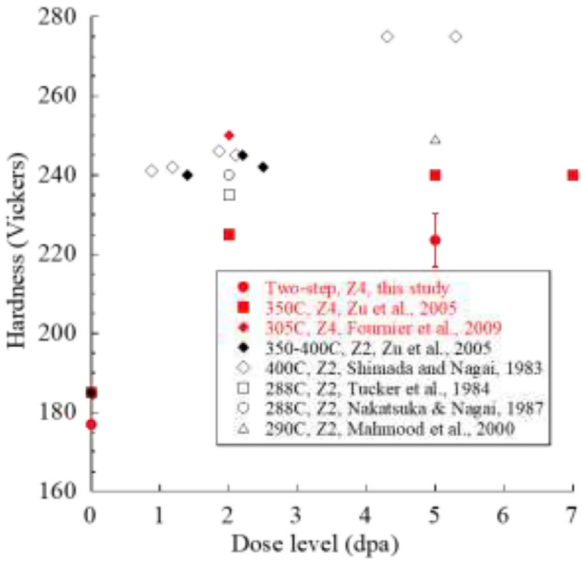


**Fig. 16.** Comparison of Vickers hardness measured in the present study and literature data for proton (solid symbols) [18,61] and neutron irradiated Zircaloy-2 [51,59,62,63](empty symbols) in the temperature range from 288 to 400 °C. The factor for converting neutron fluence to dpa is $0.6 \times 10^{25}$ n/m$^2$.

#### 4.4. Irradiation hardening

Irradiation hardening measured in this study is mostly consistent with literature data on proton irradiated experiments [18], but less than that under neutron-irradiation [59]. A comparison of hardness data between this study and other proton or neutron irradiations is presented in Fig. 16. Irradiation hardening in Zircaloy-4 increases quickly and then saturates beyond a dose of ~ 2 dpa. This behavior has also been observed by Shimada and Nagai [59] on Zircaloy-2, where the hardness value was saturated at 275 HV after neutron irradiation at 400 °C to a fluence of $3.2 \times 10^{25}$ n/m$^2$, ($E$> 1 MeV), approximately 4.6 dpa. The hardening effect that was observed in proton irradiated samples can be attributed mostly to increased <a> loop density as damage level increases at any given irradiation temperature. Cockeram et al. observed irradiation-induced hardening on neutron-irradiated Zircaloy-4 using tensile samples and also attributed the hardening effect to an increase in the number density of <a> loops [37]. The density of the <a> loop reaches a steady-state level at a neutron fluence of about $1 \times 10^{25}$ n/m$^2$ (E>1MeV), which is about 1.5 dpa [60]. The <a> loop density reaching steady-state at ~1.5 dpa under neutron irradiation also coincides with the hardness measurements obtained on proton irradiated Zircaloy in the literature and this study. At a similar dose level, the proton irradiated Zircaloy-4 demonstrates a similar transition behavior, although at slightly lower hardness values.

At higher irradiation temperatures, the hardening effect was expected to be lower than under lower temperature irradiation. Neutron irradiation conducted at higher irradiation temperatures tends to result in a larger <a> loop size and lower <a> loop number density, resulting in a lower irradiation hardening effect [37]. This has also been observed when comparing loop sizes between low-temperature isothermal proton irradiation (280–310 °C) to two-step irradiation results, where the loop size doubled in the latter irradiation. However, increased hardening was generally observed at higher irradiation temperatures, both at 330 and 350 °C, than at 280 °C and 310 °C (Fig. 12). Other microstructural or micro-

chemical evolution processes occurring during irradiation to higher doses, such as the redistribution of alloying elements from precipitates into the matrix, alloying element segregation and clustering within the matrix, and precipitation of new phases, all will contribute to hardening. Indeed, from the APT analysis of the proton irradiated samples in this study, increased Fe clustering at higher dose levels is observed, especially at the higher irradiation temperatures, as shown in Fig. 7b. The fact that increased irradiation hardening occurs under proton irradiation with increasing irradiation temperature may further indicate that increased clustering is occurring under the higher temperature proton irradiation conditions, with increased iron levels leaving the SPPs and entering the matrix.

## 5. Conclusion

The significant findings related to the capability of proton irradiation to emulate neutron irradiations microstructural and microchemical effects in Zircaloy-4 are as follows:

Isothermal proton irradiation in the temperature range of 250–350°C produces <a> and <c> type dislocation loops (in terms of morphologies and sizes) in the Zr matrix similar to that observed under neutron irradiation at these temperatures, irradiated to similar dpa levels. Under isothermal proton irradiation, both <a> and <c>-loop densities were slightly higher than neutron irradiation data. The dislocation microstructures observed on isothermally irradiated samples resulted in an increase of hardness of the sample, generally consistent with the neutron data. However, only a small fraction of each SPP was amorphized at the matrix/SPP interface, significantly less than the neutron data, especially when compared to lower neutron irradiation temperatures (260 °C to 310 °C). This also manifests in a smaller amount of Fe and Cr redistributing out of the SPPs into the surrounding matrix than occurs under neutron irradiation.

The two-step proton irradiation sequence produced complete amorphization of the SPPs and Fe redistribution into the matrix that was in good agreement with that after neutron irradiation at the lower end of the LWR operating temperature range. <a>-loop alignment in the matrix and Fe-rich rafts formation near the SPP was also apparent after a two-step irradiation sequence, similar to neutron irradiation results. The measured <a>-loop number density was comparable to neutron irradiation, with a slightly larger loop size, producing a similar hardening behavior. <c>-loop size was consistent with neutron irradiation data, with a higher loop density.

The two-step proton irradiation not only produced damage structures and irradiation hardening effects that were seen in isothermal irradiations, it also enhanced amorphization and Fe redistribution of the SPP. Hence, the two-step proton irradiation best emulates the neutron irradiated microstructure of Zircaloy-4 at the lower end of the LWR operating temperature range.

## Declaration of Competing Interest

The authors declare that they have no known competing financial interests or personal relationships that could have appeared to influence the work reported in this paper.

## CRediT authorship contribution statement

**Peng Wang:** Writing – original draft, Writing – review & editing, Investigation, Data curation, Visualization, Methodology. **Josh Bowman:** Investigation, Data curation. **Mukesh Bachhav:** Investigation, Visualization, Data curation. **Bruce Kammenzind:** Writing – review & editing, Funding acquisition, Conceptualization, Resources, Project administration. **Richard Smith:** Investigation, Funding acquisition. **Jesse Carter:** Investigation. **Arthur Motta:** Writing – review & editing, Investigation, Supervision, Funding acquisition. **Evrard Lacroix:** Investigation. **Gary Was:** Writing – review & editing, Investigation, Supervision, Funding acquisition, Project administration, Methodology, Resources.

## Acknowledgment

This work was supported by Fluor Marine Propulsion, LLC under Contract No. DOE-89233018CNR000004 with the U.S. Department of Energy (DOE), and the INL Laboratory Directed Research& Development (LDRD) Program under DOE Idaho Operations Office Contract DE-AC07-05ID14517. Mukesh N. Bachhav would like to acknowledge the Center for Advanced Energy Studies (CAES) facility for APT work awarded through NSUF-RTE program.

## References

[1] B.F. Kammenzind, J.A. Gruber, R. Bajaj, J.D. Smee, Neutron Irradiation Effects on the Corrosion of Zircaloy-4 in a Pressurized Water Reactor Environment, in: Zirconium in the Nuclear Industry: 18th International Symposium, STP 1597, ASTM International, West Conshohocken, PA, 2018, pp. 448–490, doi:10.1520/STP159720160085. in:STP1597.

[2] F. Garzarolli, Y. Broy, R. Busch, Comparison of the long-time corrosion behavior of certain Zr alloys in PWR, BWR, and laboratory tests, in: Zirconium in the Nuclear Industry: Eleventh International Symposium, STP 1295, ASTM International, West Conshohocken, PA, 1996, pp. 850–864.

[3] M. Reyes, P. Wang, G. Was, J. Marian, Determination of dose rate effects on Zircaloy oxidation using proton irradiation and oxygen transport modeling, J. Nucl. Mater. 523 (2019) 56–65, doi:10.1016/j.jnucmat.2019.05.039.

[4] B. Cox, Some thoughts on the mechanisms of in-reactor corrosion of zirconium alloys, J. Nucl. Mater. 336 (2005) 331–368, doi:10.1016/j.jnucmat.2004.09.029.

[5] A. Garde, Enhancement of aqueous corrosion of Zircaloy-4 Due to hydride precipitation at the metal-oxide interface, Zirconium in the Nuclear Industry: Ninth International Symposium, West Conshohocken, PA, 1991 ASTM International, 100 Barr Harbor Drive, PO Box C70019428-2959566-566–26, doi:10.1520/STP25527S.

[6] M. Blat, D. Noel, Detrimental Role of Hydrogen on the Corrosion rate of Zirconium Alloys, in: Zirconium in the Nuclear Industry: Eleventh International Symposium, STP1295, ASTM International, West Conshohocken, PA, 1996, pp. 319–336.

[7] M. Tupin, C. Bisor, P. Bossis, J. Chêne, J.L. Bechade, F. Jomard, Mechanism of corrosion of zirconium hydride and impact of precipitated hydrides on the Zircaloy-4 corrosion behaviour, Corros. Sci. 98 (2015) 478–493, doi:10.1016/j.corsci.2015.05.058.

[8] B. Ensor, A.M. Lucente, M.J. Frederick, J. Sutliff, A.T. Motta, The role of hydrogen in zirconium alloy corrosion, J. Nucl. Mater. 496 (2017) 301–312, doi:10.1016/j.jnucmat.2017.08.046.

[9] B. Cox, C.G. Wu, Dissolution of Zirconium-oxide films in 300-degree-C LiOH, J. Nucl. Mater. 199 (1993) 272–284.

[10] D. Pêcheur, J. Godlewski, J. Peybernès, L. Fayette, M. Noé, A. Frichet, O. Kerrec, Contribution to the Understanding of the Effect of the Water Chemistry on the Oxidation Kinetics of Zircaloy-4 Cladding, in: Zirconium in the Nuclear Industry: Twelfth International Symposium, STP 1354, ASTM International, West Conshohocken, PA, 2000, pp. 793–811. in:.

[11] B.X. Zhou, Q. Li, M.Y. Yao, W.Q. Liu, Y.L. Chu, Effect of Water Chemistry and Composition on Microstructural Evolution of Oxide on Zr Alloys, in: Zirconium in the Nuclear Industry: 15th International Symposium, STP 1505, ASTM International, West Conshohocken, PA, 2009, pp. 360–383, doi:10.1520/stp48145s.

[12] F. Garzarolli, W. Jung, H. Schoenfeld, A.M. Garde, G.W. Pary, P.G. Smerd, Waterside corrosion of Zircaloy fuel rods, Electr. Power Res. Inst. EPRI NP. (1982).

[13] B.-C. Cheng, R. Kruger, R. Adamson, Corrosion behavior of irradiated Zircaloy, Zirconium in the Nuclear Industry: Tenth International Symposium in:, West Conshohocken, PA, 2009 ASTM International, 100 Barr Harbor Drive, PO Box C70019428-2959400-400–19, doi:10.1520/stp15200s.

[14] D.M. Rishel, B.F. Kammenzind, The Role of Gamma Radiation on Zircaloy-4 Corrosion, in: Zirconium in the Nuclear Industry: 18th International Symposium, STP 1597, ASTM International, West Conshohocken, PA, 2018, pp. 555–595, doi:10.1520/STP159720160029.

[15] E.M. Francis, A. Harte, P. Frankel, S.J. Haigh, D. Jädernäs, J. Romero, L. Hallstadius, M. Preuss, Iron redistribution in a zirconium alloy after neutron and proton irradiation studied by energy-dispersive X-ray spectroscopy (EDX) using an aberration-corrected (scanning) transmission electron microscope, J. Nucl. Mater. 454 (2014) 387–397, doi:10.1016/j.jnucmat.2014.08.034.

[16] A. Harte, M. Topping, P. Frankel, D. Jädernäs, J. Romero, L. Hallstadius, E.C. Darby, M. Preuss, Nano-scale chemical evolution in a proton-and neutron-irradiated Zr alloy, J. Nucl. Mater. 487 (2017) 30–42, doi:10.1016/j.jnucmat.2017.01.049.

[17] M. Topping, A. Harte, T. Ungár, C.P. Race, S. Dumbill, P. Frankel, M. Preuss, The effect of irradiation temperature on damage structures in proton-irradiated zirconium alloys, J. Nucl. Mater. 514 (2019) 358–367, doi:10.1016/j.jnucmat.2018.12.006.

[18] X.T. Zu, K. Sun, M. Atzmon, L.M. Wang, L.P. You, F.R. Wan, J.T. Busby, G.S. Was, R.B. Adamson, Effect of proton and Ne irradiation on the microstructure of Zircaloy 4, Philos. Mag. (2005) 649–659, doi:10.1080/14786430412331320017.
[19] G.S. Was, S.J. Zinkle, Toward the use of ion irradiation to predict reactor irradiation effects, in: Comprehensive Nuclear Materials, Elsevier, 2020, pp. 468–484.
[20] G.S.S. Was, R.S. Averback, Chapter 7 radiation damage using ion beams, in: R. Konings (Ed.), Comprehensive Nuclear Materials, Elsevier B.V., 2012.
[21] G.S. Was, T.R. Allen, Radiation damage from different particle types, in: Radiation Effects in Solids - NATO Science Series II - Mathematics, Physics and Chemistry, 235, Springer, Berlin, Germany, 2007, pp. 65–98.
[22] C. Yan, R. Wang, Y. Wang, X. Wang, G. Bai, Effects of ion irradiation on microstructure and properties of zirconium alloys: a review, Nucl. Eng. Technol. 47 (2015) 323–331, doi:10.1016/j.net.2014.12.015.
[23] D. Charquet, E. Steinberg, Y. Millet, Influence of variations in early fabrication steps on corrosion, mechanical properties, and structure of Zircaloy-4 products, in: Zirconium in the Nuclear Industry: Seventh International Symposium, STP 939, ASTM International, West Conshohocken, PA, 1987, pp. 431–447.
[24] R. Bajaj, B.F. Kammenzind, D.M. Farkas, Effects of Neutron Irradiation on the Microstructure of Alpha-Annealed Zircaloy-4, in: Zirconium in the Nuclear Industry: Thirteenth International Symposium, STP 1423, ASTM International, West Conshohocken, PA, 2002, pp. 400–425, doi:10.1520/stp11399s.
[25] K.R. Anderson, R. Bajaj, Microstructural and microchemical analyses of extracted second-phase precipitates in alpha-annealed and beta-quenched Zircaloy-4, Microsc. Microanal. 20 (2014) 500–501, doi:10.1017/S143192761400422X.
[26] R.E. Stoller, M.B. Toloczko, G.S. Was, A.G. Certain, S. Dwaraknath, F.A. Garner, On the use of SRIM for computing radiation damage exposure, Nucl. Instrum. Methods Phys. Res. Sect. B Beam Interact. Mater. Atoms 310 (2013) 75–80, doi:10.1016/j.nimb.2013.05.008.
[27] J. Ziegler, M. Ziegler, J. Biersack, SRIM - The Stopping and Range of Ions in Matter (2010), SRIM Co., 2008 Computer Program.
[28] S.M. Hanlon, S.Y. Persaud, F. Long, A. Korinek, M.R. Daymond, A solution to FIB induced artefact hydrides in Zr alloys, J. Nucl. Mater. (2019), doi:10.1016/j.jnucmat.2018.12.020.
[29] G. Cliff, G.W. Lorimer, The quantitative analysis of thin specimens, J. Microsc. 103 (1975) 203–207, doi:10.1111/j.1365-2818.1975.tb03895.x.
[30] G. Cao, Y. Yun, L. Yang, G. Yuan, Q. Yue, G. Shao, J. Hu, The formation and stacking faults of Fe and Cr containing laves phase in Zircaloy-4 alloy, Mater. Lett. 191 (2017) 203–205, doi:10.1016/j.matlet.2016.12.062.
[31] Y. Idrees, Z. Yao, M. Sattari, M.A. Kirk, M.R. Daymond, Irradiation induced microstructural changes in Zr-Excel alloy, J. Nucl. Mater. (2013), doi:10.1016/j.jnucmat.2013.05.036.
[32] A. Harte, D. Jädernäs, M. Topping, P. Frankel, C.P. Race, J. Romero, L. Hallstadius, E.C. Darby, M. Preuss, The effect of matrix chemistry on dislocation evolution in an irradiated Zr alloy, Acta Mater. 130 (2017) 69–82, doi:10.1016/j.actamat.2017.03.024.
[33] A. Harte, M. Griffiths, M. Preuss, The characterisation of second phases in the Zr-Nb and Zr-Nb-Sn-Fe alloys: a critical review, J. Nucl. Mater. 505 (2018) 227–239, doi:10.1016/j.jnucmat.2018.03.030.
[34] D.O. Northwood, R.W. Gilbert, L.E. Bahen, P.M. Kelly, R.G. Blake, A. Jostsons, P.K. Madden, D. Faulkner, W. Bell, R.B. Adamson, Characterization of neutron irradiation damage in zirconium alloys - an international "round-robin" experiment, J. Nucl. Mater. 79 (1979) 379–394, doi:10.1016/0022-3115(79)90103-X.
[35] M. Griffiths, A review of microstructure evolution in zirconium alloys during irradiation, J. Nucl. Mater. 159 (1988) 190–218, doi:10.1016/0022-3115(88)90093-1.
[36] A. Jostsons, P.M. Kelly, R.G. Blake, K. Farrell, Neutron Irradiation-Induced Defect Structures in Zirconium, in: Effects of Radiation on Structural Materials, STP 683, ASTM International, West Conshohocken, PA, 1979, pp. 46–61.
[37] B.V. Cockeram, K.J. Leonard, T.S. Byun, L.L. Snead, J.L. Hollenbeck, Development of microstructure and irradiation hardening of Zircaloy during low dose neutron irradiation at nominally 377–440°C, J. Nucl. Mater. 449 (2014) 69–87, doi:10.1016/j.jnucmat.2014.03.004.
[38] Y. Etoh, S. Shimada, Neutron irradiation effects on intermetallic precipitates in Zircaloy as a function of fluence, J. Nucl. Mater. 200 (1993) 59–69, doi:10.1016/0022-3115(93)90009-N.
[39] M. Griffiths, R.W. Gilbert, G.J.C. Carpenter, Phase instability, decomposition and redistribution of intermetallic precipitates in Zircaloy-2 and -4 during neutron irradiation, J. Nucl. Mater. 150 (1987) 53–66, doi:10.1016/0022-3115(87)90093-6.
[40] M. Griffiths, Comments on precipitate stability in neutron-irradiated Zircaloy-4, J. Nucl. Mater. 170 (1990) 294–300, doi:10.1016/0022-3115(90)90302-4.
[41] D. Gilbon, C. Simonot, Effect of irradiation on the microstructure of Zircaloy-4, in: Zirconium in the Nuclear Industry: Tenth International Symposium, STP 1245, ASTM International, West Conshohocken, PA, 1994, pp. 521–548. 521-521–28.
[42] A.T. Motta, Mechanistic Understanding of Zirconium Alloy Fuel Cladding Performance, in: Zirconium in the Nuclear Industry: 18th International Symposium, STP 1597, ASTM International, West Conshohocken, PA, 2018, pp. 19–51, doi:10.1520/STP159720160095.
[43] L. Walters, S.R. Douglas, M. Griffiths, Equivalent radiation damage in zirconium irradiated in various reactors, in: R.J. Comstock (Ed.), Zirconium in the Nuclear Industry: 18th International Symposium, STP 1597, ASTM International, West Conshohocken, PA, 2018, pp. 676–690.
[44] S.X. Wang, L.M. Wang, R.C. Ewing, Irradiation-induced amorphization: Effects of temperature, ion mass, cascade size, and dose rate, Phys. Rev. B Condens. Matter Mater. Phys. (2001), doi:10.1103/PhysRevB.63.024105.
[45] G.S. Was, Fundamentals of Radiation Materials Science: Metals and Alloys, Fundamentals of Radiation Materials Science: Metals and Alloys, 2nd Ed., Springer New York, 2016.
[46] G. Hood, R. Schultz, Diffusion of 3D transition elements in $\alpha$-Zr and Zirconium alloys, in: Zirconium in the Nuclear Industry: Eighth International Symposium, STP 1023, ASTM International, West Conshohocken, PA, 1989, pp. 435–450. 435-435-16.
[47] M. Topping, A. Harte, P. Frankel, C. Race, G. Sundell, M. Thuvander, H.O. Andrén, D. Jadernas, P. Tejland, J.E. Romero, E.C. Darby, S. Dumbill, L. Hallstadius, M. Preuss, The Effect of Iron on Dislocation Evolution in Model and Commercial Zirconium Alloys, in: Zirconium in the Nuclear Industry: 18th International Symposium, STP 1597, ASTM International, West Conshohocken, PA, 2018, pp. 796–822.
[48] G. Sundell, M. Thuvander, P. Tejland, M. Dahlbäck, L. Hallstadius, H.-O. Andrén, Redistribution of alloying elements in Zircaloy-2 after in-reactor exposure, J. Nucl. Mater. 454 (2014) 178–185, doi:10.1016/j.jnucmat.2014.07.072.
[49] R.P. Agarwala, M.S. Anand, B.M. Pande, Radiation damage in zirconium and its alloys, Defect Diffus. Forum 48 (1987) 29–56, doi:10.4028/www.scientific.net/DDF.48.29.
[50] B.V. Cockeram, P.D. Edmondson, K.J. Leonard, B.F. Kammenzind, J.L. Hollenbeck, Atom probe examinations of Zircaloy irradiated at nominally 358°C, Nucl. Mater. Energy. 19 (2019) 416–432, doi:10.1016/j.nme.2019.03.023.
[51] S.T. Mahmood, D.M. Farkas, R.B. Adamson, Y. Etoh, Post-irradiation Characterization of Ultra-high-fluence Zircaloy-2 plate, in: Zirconium in the Nuclear Industry: Twelfth International Symposium, STP 1354, ASTM Internatinal, West Conshohocken, PA, 2000, pp. 139–169, doi:10.1520/stp14299s.
[52] L. Tournadre, F. Onimus, J.L. Béchade, D. Gilbon, J.M. Cloué, J.P. Mardon, X. Feaugas, O. Toader, C. Bachelet, Experimental study of the nucleation and growth of c-component loops under charged particle irradiations of recrystallized Zircaloy-4, J. Nucl. Mater. (2012), doi:10.1016/j.jnucmat.2011.11.061.
[53] M. Griffiths, R.W. Gilbert, The formation of c-component defects in zirconium alloys during neutron irradiation, J. Nucl. Mater. 150 (1987) 169–181, doi:10.1016/0022-3115(87)90072-9.
[54] R. Adamson, W. Bell, D. Lee, Use of ion bombardment to study irradiation damage in zirconium alloys, in: Zirconium in Nuclear Applications, STP 551, ASTM International, West Conshohocken, PA, 1974, pp. 215–228, doi:10.1520/STP32117S.
[55] A.T. Motta, K.T. Erwin, O. Delaire, R.C. Birtcher, Y. Chu, J. Maser, D.C. Mancini, B. Lai, Synchrotron Radiation Study of Second Phase Particles and Alloying Elements in Zirconium Alloys, in: Zirconium in the Nuclear Industry: Thirteenth International Symposium, STP 1423, ASTM International, West Conshohocken, PA, 2002, pp. 59–77, doi:10.1520/stp11383s.
[56] R.M. Kruger, R.B. Adamson, S.S. Brenner, Effects of microchemistry and precipitate size on nodular corrosion resistance of Zircaloy-2, J. Nucl. Mater. 189 (1992) 193–200, doi:10.1016/0022-3115(92)90532-P.
[57] R.A. Holt, R.W. Gilbert, <c>Component dislocations in annealed Zircaloy irradiated at about 570 K, J. Nucl. Mater. 137 (1986) 185–189, doi:10.1016/0022-3115(86)90218-7.
[58] T. Sawabe, T. Sonoda, S. Kitajima, T. Kameyama, Analysis of atomic distribution in as-fabricated Zircaloy-2 claddings by atom probe tomography under high-energy pulsed laser, J. Nucl. Mater. 442 (2013) 168–174, doi:10.1016/j.jnucmat.2013.08.048.
[59] S. Shimada, M. Nagai, Evaluation of the resistance of irradiated zirconium-liner cladding to iodine-induced stress corrosion cracking, J. Nucl. Mater. 114 (1983) 305–311, doi:10.1016/0022-3115(83)90269-6.
[60] R.B. Adamson, B. Cox, Impact of irradiation on material performance, ZIRAT-10 Special Topics Report, Advanced Nuclear Technology International, Ekbacken 33 SE-735 35 SURAHAMMAR Sweden, 2005.
[61] L. Fournier, A. Serres, Q. Auzoux, D. Leboulch, G.S. Was, Proton irradiation effect on microstructure, strain localization and iodine-induced stress corrosion cracking in Zircaloy-4, J. Nucl. Mater. 384 (2009) 38–47, doi:10.1016/j.jnucmat.2008.10.001.
[62] R.P. Tucker, R.B. Adamson, Irradiation hardening as measured by microhardness, 1984.
[63] M. Nakatsuka, M. Nagai, Reduction of plastic anisotropy of zircaloy cladding by neutron irradiation. (I). Yield loci obtained from knoop hardness, J. Nucl. Sci. Technol. 24 (1987) 832–838, doi:10.3327/jnst.24.832.